Journal of Alloys and Compounds 505 (2010) 555–559

Contents lists available at ScienceDirect

Journal of Alloys and Compounds

journal homepage: www.elsevier.com/locate/jallcom

Nanostructured amorphous MnO_2 prepared by reaction of $KMnO_4$ with triethanolamine

Yan-jing Yang, En-hui Liu*, Li-min Li, Zheng-zheng Huang, Hai-jie Shen, Xiao-xia Xiang

Key Laboratory of Environmentally Friendly Chemistry and Applications of Ministry of Education, College of Chemistry, Xiangtan University, Xiangtan, Hunan 411105, PR China

ARTICLE INFO

Article history:
Received 24 November 2009
Received in revised form 9 June 2010
Accepted 11 June 2010
Available online 23 June 2010

Keywords:
Manganese oxides
Heat-treatment
Supercapacitor
Electrochemical properties

ABSTRACT

Amorphous manganese dioxide is prepared by reaction of potassium permanganate with an organic reductant triethanolamine. The effect of heat-treatment temperature is studied on the characteristics of the materials. Power X-ray diffraction (XRD), scanning electron microscope (SEM) and N_2 adsorption and desorption measurements are employed to investigate crystalline structure, surface morphology, the specific surface area and the pore size distribution. It is found that when the annealing temperature reaches up to 400 °C, the crystalline convert to α-MnO_2 from amorphous MnO_2. The electrochemical characteristics of the prepared MnO_2 powder are characterized by means of cyclic voltammetry (CV), experiments in 1.0 mol L^{-1} Na_2SO_4 electrolyte. The specific capacitance (SC) value is 251 F g^{-1} that is obtained from the product annealing at 350 °C at a CV scan rate of 2 mV s^{-1}. And charging–discharging measurement reveals the good stability of the prepared material.

1. Introduction

Supercapacitors (or eletrochemical capacitors) have recently drawn much attention as energy storage devices due to their higher power density and long cycle life compared to secondary batteries and higher energy density than conventional capacitors [1–3]. According to the charge storage mechanism they can be classified into two types: One is electrochemical double-layer capacitor (EDLC) which exhibits a non-faradic reaction with accumulation of charges at the interface between the electrode and the electrolyte. The electrodes mainly focus on carbon-based materials [4,5]. The other is pseudocapacitor which stores energy by the process of faradic redox reaction [6–8].

The psuedocapacitors based on transition oxides (such as $RuO{\cdot}nH_2O$, CoO_x, MnO_2, NiO, etc.) have attracted significant attention owing to their high specific capacitance, excellent reversibility and long cycle life. Although supercapacitors based on $RuO_2{\cdot}nH_2O$ exhibit a large specific capacitance of as 750 F g^{-1} in acid electrolyte [9], its high cost and toxicity limit it from commercialization [10]. Consequently, researchers have been searching an alternative for $RuO_2{\cdot}nH_2O$ all the time. Metal oxide MnO_2 with its low cost, friendly environmental and richness in nature has been investigated to be a promising candidate as supercapacitor material [11].

There are usually two charge/discharge mechanisms in MnO_2-based supercapacitor in aqueous electrolyte. One is intercalation/deintercalation (i/d) of cations (such as Li^+, Na^+, K^+) or/and protons (H_3O^+) into the bulk of MnO_2, which may be described by the redox reaction:

$$MnO_2 + C^+ + e^- \rightleftharpoons MnOOC(M = Li^+, Na^+, K^+ \text{ or } H_3O^+) \quad (1)$$

The second mechanism is a surface adsorption/desorption (a/d) process of cations or/and protons from the electrolyte:

$$(MnO_2)_{surface} + C^+ + e^- \rightleftharpoons (MnOOC)_{surface}(C^+ = Li^+, Na^+, K^+ \text{ or } H_3O^+) \quad (2)$$

The i/d process is expected to take place in the crystalline MnO_2, while the a/d process mainly occurs in the amorphous MnO_2 [12,13].

Manganese oxides have been prepared by many different methods such as hydrothermal synthesis [14,15], sol–gel [16,17], thermal decomposition [18], coprecipitation [19], electrochemical deposition [20,21] and so on. Liang and Hwang [9] reported that a capacitance of 244 F g^{-1} and good stability was obtained of hydrous manganese oxide in Na_2SO_4 solution. Huang et al. [15] prepared β-MnO_2 by hydrothermal synthesis and obtained an initial discharge capacity of 251 mAh g^{-1} when applied in lithium battery. Babakhani and Ivey [21] obtained manganese oxide with rod-like structures and researched its properties as supercapacitor electrode material, the results showed a capacitance of 185 F g^{-1}.

Among these methods, the main advantage of hydrothermal synthesis is that interesting nanostructure (such as nanowires, nanorods, nanochins and so forth) can be tailored by controlling the temperature and time of the reaction, but the SC value is lower. Although sol–gel and coprecipitation methods can gain high SC val-

* Corresponding author. Tel.: +86 731 58292229; fax: +86 731 58292477.
E-mail address: liuenhui99@sina.com.cn (E.-h. Liu).

0925-8388/$ – see front matter © 2010 Elsevier B.V. All rights reserved.
doi:10.1016/j.jallcom.2010.06.072

ues materials, the multiple prepared steps are required. It is thin films electrodes that are usually obtained by electrochemical deposition, which may suffer from poor energy density.

In this paper, we prepared MnO_2 through a simple precipitation technique. Poor crystalline nanostructured MnO_2 was synthesized by reduction of $KMnO_4$ with an organic reductant triethanolamine and annealed at 300, 350, 400 °C, respectively. The structure, surface morphology, specific surface area and electrochemical performance of prepared products are presented and discussed. To the best of our knowledge, it has not been reported that using triethanolamine as reducing agent to synthesis manganese dioxide. Furthermore, $KMnO_4$ is the only one starting manganese precursor in our approach, the organic reductant used here has the merits of simple steps, less sample consumption and high yield, which are advantages when considered for commercial purposes.

2. Experimental

2.1. Synthesis of manganese dioxide material

All chemicals were analytical grade and were used without further purification. All aqueous solutions were prepared using distilled water.

In a typical synthesis process, 1.7 mL triethanolamine was diluted in 100 mL distilled water followed by 200 mL 0.03 mol L^{-1} $KMnO_4$ added drop-wise with vigorous stirring. After stirring for a period of time at room temperature, the stirring was terminated and a brown precipitate was obtained. The precipitate was filtered and washed with distilled water until the pH of the washed water is 7.

The reaction of synthesis MnO_2 was displayed below:

$$4KMnO_4 + N(CH_2CH_2OH)_3 \rightarrow 4MnO_2 + K_2C_2O_4 + 2CH_3COOK + NH_3 + 3H_2O$$

$KMnO_4$, the only source here containing manganese and oxidizing agent, was reduced by triethanolamine, which lead to the formation of manganese dioxide.

Then the precipitate was dried at 100 °C for 24 h. Subsequently, part of the powder was annealed 2 h at 300, 350 and 400 °C, respectively. The samples were denoted as MN100, MN300, MN350, and MN400 in the following paragraphs.

2.2. Characterization

The XRD was employed to study the crystallographic characteristics of synthesized samples by a diffractometer (D/MAX-3C) with Cu Kα ($\lambda = 1.5406$ Å) as radiation. SEM studies were examined on a LEO 1525 microscopy to investigate the surface morphology of the prepared materials. The surface area of MnO_2 was studied by BET measurement by nitrogen gas adsorption–desorption method at 77 K using a NOVA2200 (Quantachrome) automatic adsorption unit.

2.3. Preparation of the electrodes

The electrode consisted of 80% active material (MN100, MN300, MN350, or MN400) powder, 10% acetylene black (AB) as conducting agent, and 10% polyvinylidene fluoride (PVDF) as a binder. First, PVDF was dissolved in N-methyl-2-pyrrolidone (NMP), then AB and active material were mixed orderly to form a homogeneous slurry, which was subsequently blush-coated onto nickel foam current collectors ($\Phi = 10$ mm) and dried at 100 °C for 12 h to fabricate electrodes. Mass of the active materials of each electrode was about 10 mg.

All the electrochemical measurements were completed in 1.0 mol L^{-1} Na_2SO_4 electrolyte, and electrochemical characteristics were carried out at CHI660A electrochemical workstation (CH Instruments, USA).

3. Results and discussion

3.1. Material characteristics

Power XRD was employed to analyze the structures. Fig. 1 shows the XRD patterns of MN100, MN300, MN350 and MN400. Fig. 1a–c are similar and only a few broad peaks are appeared. Those broadening peak features indicate the amorphous nature of MN100, MN300 and MN350. Broad peaks at $2\theta = 36.9°$ and 66.3° are present. There is a transformation in crystallinity when post-treat temperature reached up to 400 °C with the appearance of clear sharp peaks. As can be see from Fig. 1d, the sharp peaks at $2\theta = 12.7°$, 18.0°, 28.6°, 37.5°, 41.9°, 49.7°, 60.1°, and 69.3° corresponding to α-MnO_2 matched with JCPDS 44-0141 [6,12].

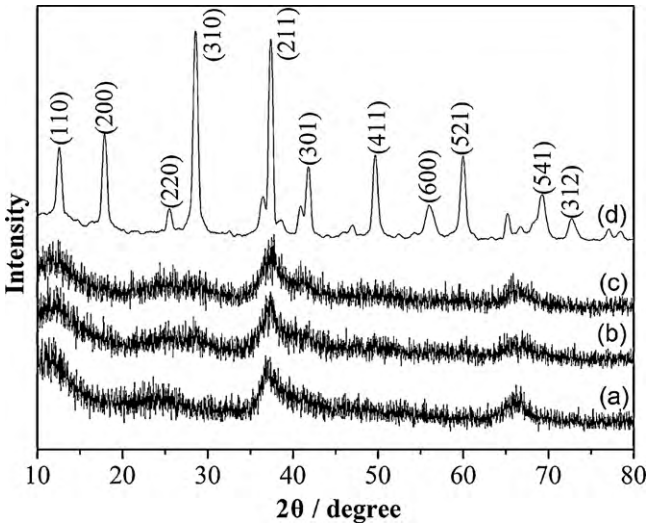

Fig. 1. XRD patterns of MN100 (a), MN300 (b), MN350 (c) and MN400 (d).

Surface morphology images of the synthesized MnO_2 materials were examined by SEM microscope. Fig. 2 depicts the photomicrographs of MN100, MN300, MN350 and MN400. As shown in Fig. 2a, a mass of particles agglomerates together and forms big conglomerates on the MN100 surface. For the annealed samples, the macro-agglomerates have been dispersed to a certain degree. The morphology of MN300 (Fig. 2b) is composed of nanoparticles with an average diameter of about 11 nm. It is found that the surface of MN350 (Fig. 2c) is characterized by abundant particles connecting with each other and forming the porous properties. It provides the locale for cations reaching into MnO_2 bulk when the process of intercalation/deintercalation took place. The diameters of the nanoparticles ranged from 17–32 nm with an average of 25 nm are observed for MN400 (Fig. 2d). The heat-treatment changed the morphology and increased the average diameter of the MnO_2 powders.

N_2 adsorption–desorption measurement was employed to determine the specific surface area and the pore size distribution of the prepared samples. The specific surface area, total pore volume, and specific capacitance of synthesized MnO_2 powders are indicated in Table 1. The BET surface area was obtained to be 65 m^2 g^{-1} for the MN100. And there is a little decrease in specific surface area of annealed materials, which are 49, 57 and 48 m^2 g^{-1} for MN300, MN350 and MN400, respectively. Fig. 3 shows the N_2 adsorption and desorption of samples heat-treated at different temperature. For MN300 and MN350, the N_2 adsorption and desorption curves form hysteresis loops, exhibiting a H_3-type of IV-type according to IUPAC, which is characteristic of mesoporous solids. For MN100 and MN400, the fraction of mesopores is not so large because the hysteresis loops are not so clear and with less amount of N_2 absorbed [22]. Pore size distribution curves of MN100, MN300, MN350 and MN400 are shown in Fig. 4. According to IUPAC nomenclature, micropores are less than 2 nm in diameter, mesopores are between 2 and 50 nm in diameter, and macropores are greater than 50 nm in diameter. For MN100, the peaks with mean pore widths of around 1.3–4 nm some around 10 nm were emerged (Fig. 4). As temperature increasing, the peaks of MN100's pore size distribution curve changed to increase. The enhanced peaks may be attributed to exposure of new pores that were occupied by water and some small organic molecules before heat-treatment. And for MN300 and MN350, a broad distribution was found in the mesopore region, and both of the two curves have low broad peaks centered at about 10 nm. But due to the point-to-point nature of the experimental data in Fig. 3, the curves in Fig. 4 are not smooth.

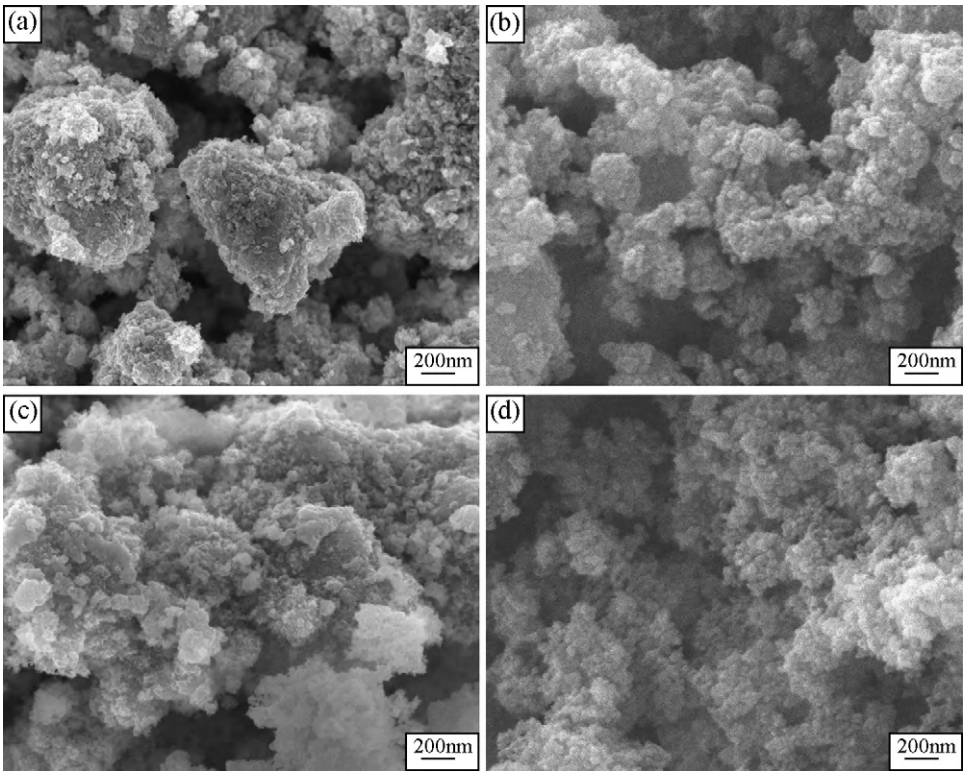

Fig. 2. SEM images of MN100 (a), MN300 (b), MN350 (c), and MN400 (d).

Table 1
Specific surface area, total pore volume and specific capacitance of prepared MnO_2.

Sample	Specific surface area ($m^2\,g^{-1}$)	Total pore volume ($cc\,g^{-1}$)	Specific capacitance ($F\,g^{-1}$)
MN100	65	0.172	169
MN300	49	0.166	182
MN350	57	0.192	251
MN400	48	0.116	153

And when temperature reached up to 400 °C, pore size distribution was scattered and surface area decreased, the reason may be due to that the pores collapsed during the high-temperature heat-treatment [23].

3.2. Electrochemical studies

The cyclic voltammetry (CV) is usually considered to be a powerful tool to measure whether the material is suitable for supercapacitor or battery electrode. Fig. 5a shows the CV curves of prepared MnO_2 electrodes. The CV curves were measured in $1.0\,mol\,L^{-1}$ Na_2SO_4 electrolyte and a potential range from 0 to 1.0 V at a scan rate of $2\,mV\,s^{-1}$. The rectangular CV profile is a fingerprint indicating ideal capacitive behavior [24]. For MN100, MN300 and MN350, the voltammograms are approximately rectangular in shape. Among these samples, the highest current density is obtained for MN350. The CV curve of MN100 mingles with MN300, implying the SC values of MN100 and MN300 are similar. While the CV shape of MN400 shows a

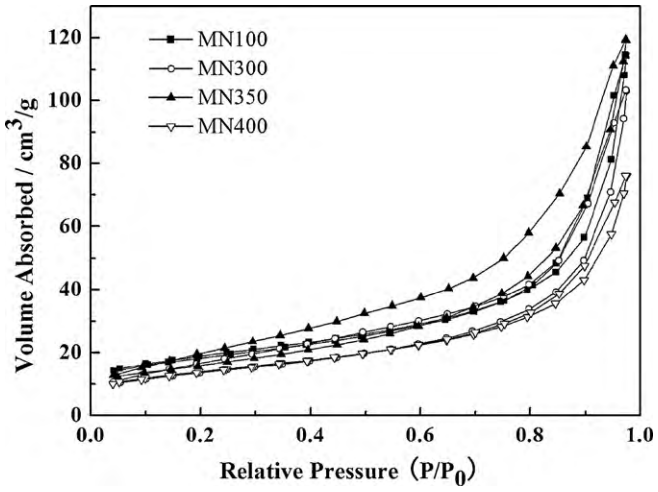

Fig. 3. N_2 adsorption–desorption results of MN100, MN300, MN350 and MN400.

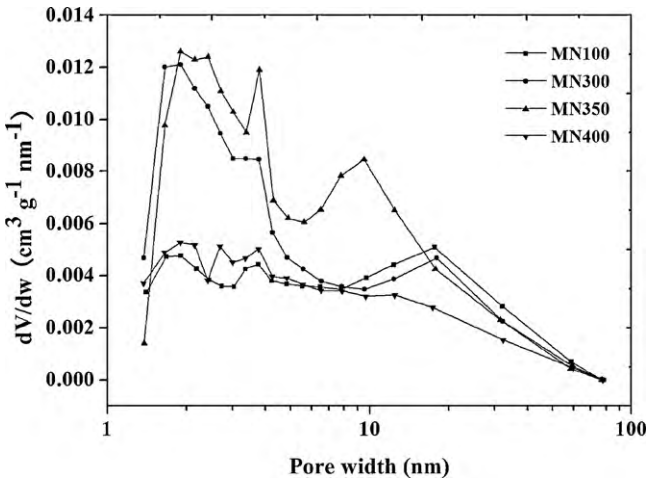

Fig. 4. Pore size distribution of MN100, MN300, MN350 and MN400.

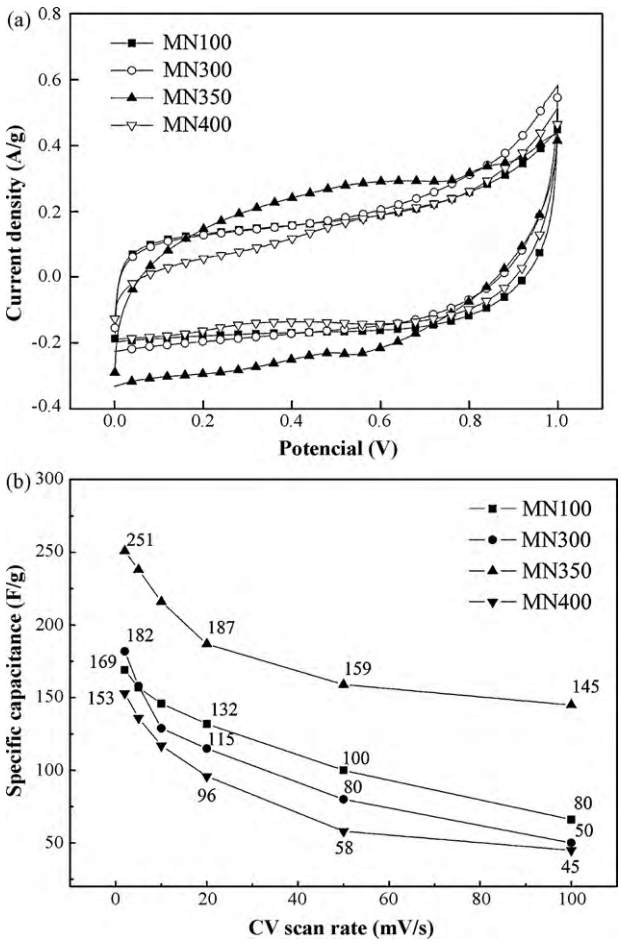

Fig. 5. (a) CV curves of prepared MnO_2 electrodes at a sweep rate of 2 mV s^{-1} in 1.0 mol L^{-1} Na_2SO_4 electrolyte. (b) Effect of post-treat temperature and CV scan rate on specific capacitance of MnO_2 electrodes.

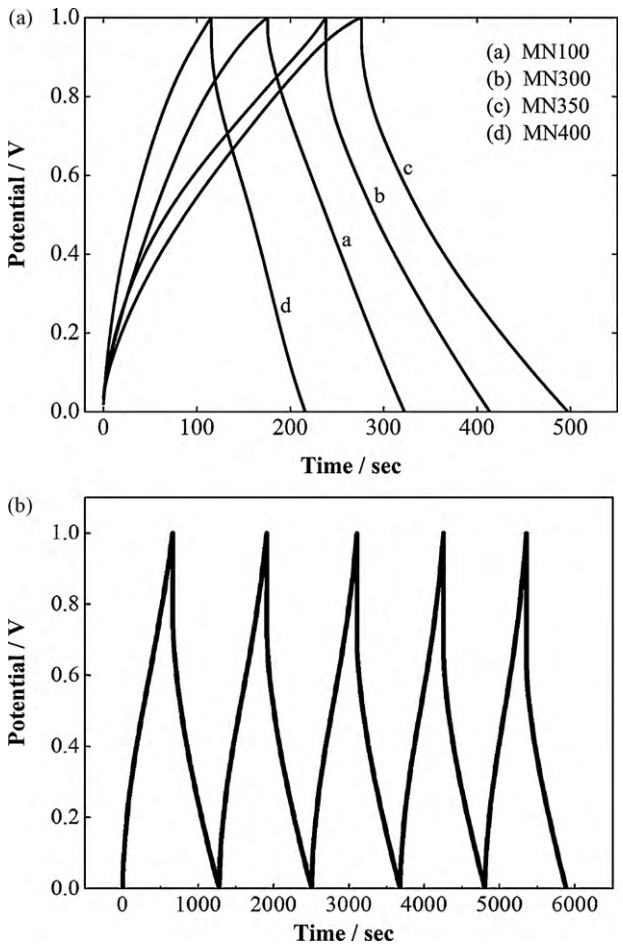

Fig. 6. (a) Galvanostatic charge–discharge curves of prepared MnO_2 electrodes in 1.0 mol L^{-1} Na_2SO_4 electrolyte between 0 and 1.0 V at a current density of 500 mA g^{-1}. (b) Charge–discharge cycles of MN350 electrode at a current density of 200 mA g^{-1} in 1.0 mol L^{-1} Na_2SO_4 solution.

deformed rectangle in the potential range studied. The current density of discharging is lower than that of charging at 1 V or so. The specific capacitance is calculated by integrating the area of the CV curves. The best result of specific capacitance value is 251 F g^{-1} that is obtained from the sample of MN350 at a scan rate of 2 mV s^{-1}. The value is comparable to that of previous reported result that powder MnO_2-based electrode capacitance is 150–300 F g^{-1} [25]. And the specific capacitances of MN100, MN300 and MN400 are 169, 182 and 153 F g^{-1}, respectively.

Fig. 5b shows the specific capacitance values of the samples at different CV scan rates. It is clearly observed that there is a decrease in SC values with an increase in sweep rate. For instance, the SC value of MN350 is 251 F g^{-1} at a scan rate of 2 mV s^{-1} and 145 F g^{-1} retains when the scan rate increases to 100 mV s^{-1}. That may be due to a loss in efficiency of utilization of active material at high sweep rate. Because there is no enough time for cations reaching into MnO_2 matrix, only reaching the outer surface at a high scan rate. Particular in a redox supercapacitor, the effective use of the material is directly bound up with the capacitance behavior.

Galvanostatic charging–discharging plots of the MnO_2 electrodes measured at a current density of 500 mA g^{-1} in a 1.0 mol L^{-1} Na_2SO_4 electrolyte are shown in Fig. 6a. The linear and symmetric characteristic is another identification indicating ideal capacitance behavior for electrode materials. It can be seen from Fig. 6a, for all the electrodes, the variation of potential with time is approximately linear in both charging and discharging process. The specific capacitance is calculated from the formulation:

$$C = \frac{It}{m\Delta V} \times 2$$

where C is the specific capacitance (F g^{-1}), I is the charging/discharging current (A), t is the charging/discharging time (s), m is the mass of one electrode active material (g) and ΔV is the potential range. The SC values calculated from the above formulation for MN100, MN300, MN350, and MN400 are147, 175, 221 and 110 F g^{-1} at a current density of 500 mA g^{-1}, respectively, which approximately match with the results calculated from CV test.

Fig. 6b shows the first several charging–discharging cycles for MN350 at a current density of 200 mA g^{-1} in 1.0 mol L^{-1} Na_2SO_4 solution. The charging time and discharging time are almost the same indicating a high charging–discharging efficiency. The specific capacitance calculated here is 247 F g^{-1} at a current density of 200 mA g^{-1} and there is hardly any decay in capacitance after several cycles.

From these different specific capacitance values, we can find that the post-treat temperature, which changed the crystalline structure, surface morphology, specific surface area value and the pore size distribution of the material, is an important factor to the material in electrochemical performance. There has been an increase in capacitance with the increase in annealed temperature, while the capacitance decreased when the temperature exceeds 350 °C. It is the advantage that large pores in mass transport and the cations in the electrolyte can transport in the macropores and meso-

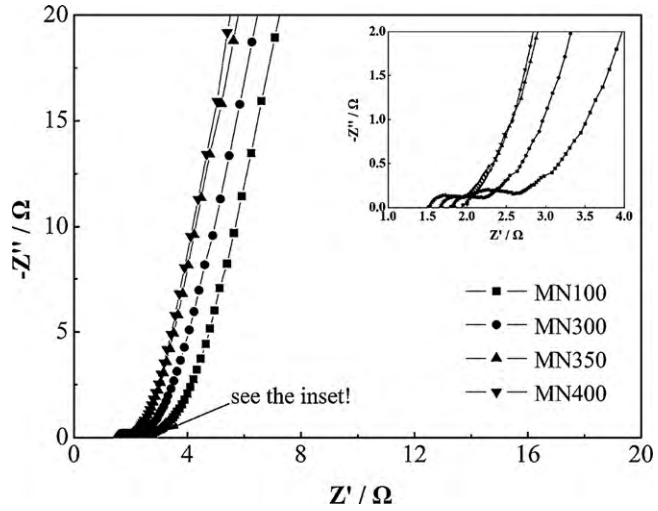

Fig. 7. Impedance plots of electrodes at 1.0 mol L^{-1} Na_2SO_4 electrolyte, frequency range from 10^5 to 0.01 Hz (inset is a local enlargement).

pores more easily and rapidly than in micropores. For the whole charge storage process of MnO_2 involving transport and insertion of cations in the electrolyte, large pore size and a wide pore size distribution in the mesopore region insure that most surface of MN300 and MN350 are immediately accessible for cations. As for the specific capacitance of MN300 lower than MN350, the only reason is the slightly higher specific surface area for MN350. For MN100 and MN400, the existence of micropores goes against the access for cations and may slow down the transport of cations. Although the specific surface area of MN350 (57 m^2 g^{-1}) is little lower than MN100 (65 m^2 g^{-1}), the pore distribution is wider and total pore volume is higher than that of MN100. That is key factors when discussing the electrochemical properties [6]. And the MN350 provides more advantageous porous structure for deintercalation upon oxidation and intercalation upon reduction process of cations into the MnO_2 matrix. The BET surface area value is not the only factor influenced the electrochemical properties, so the capacitance does not absolutely follow the trend of the BET surface area value. Similar results that higher specific capacitance with lower specific surface area were obtained in the literature [6,26,27]. The alteration in crystalline structure by high-temperature heat-treatment may lead to the variation of physical or chemical properties and cause the change in specific capacitance [28]. Lower specific surface area value and total pore volume and more narrow pore size distribution were obtained for MN400 compared to MN350.

In order to further understand the electrochemical properties of the MnO_2 electrodes, EIS was test in 1.0 mol L^{-1} Na_2SO_4 electrolyte. Fig. 7 displays the Nyquist plots for the prepared MnO_2 materials performed in a frequency range from 10^5 to 0.01 Hz. It can be observed from Fig. 6 that the impedance plots of all the electrodes are consist of a distorted semi-circle at the high-frequency region and an almost vertical linear spike at the low-frequency region. At the high-frequency region, the X-intercept yields the internal resistance R_s, while the diameter of the semi-circle provides the charge-transfer resistance (R_{ct}) of the electrode/electrolyte interface. Since we used the same electrolyte, the R_s values of MN100, MN300, MN350 and MN400 are similar to each other, which are 1.9, 1.7, 1.5 and 1.6 Ω, respectively. The charge-transfer resistance of MN100 (0.68 Ω) is higher than that of annealed materials, and it is noticeable that R_{ct} decreased as the post-treat temperature increased, following the order: MN300 > MN350 ~ MN400. It can be concluded that heat-treatment can reduce the charge-transfer resistance, which is advantageous for electrodes. At the low-frequency region, the slopes of imaginary parts of the impedance plots, associated with the capacitive behavior, increased with the annealed temperature. For an ideal capacitor, the impedance plots should be a vertical line parallel to the imaginary axis. From Fig. 6, the plot of MN350 is almost perpendicular to the real axis, indicating lower diffusive resistance for intercalation/deintercalation of cations than that of others. The EIS results reveal the better properties of MN350 that are in step with the CV results. Although the plot of MN400 nearly coincides with MN350, the electrochemical active sites would decrease when the heat-treatment temperature ≥400 °C. That may be another reason for the decreased specific capacitance of MN400. The result is in agreement with Sang-Eun Chun and his co-workers [29] who researched the effect of heat-treatment to the mechanism of charging/discharging in neutral solution by impedance spectroscopy. All the results are indicative of MN350 suitable for electrode material.

4. Conclusions

Amorphous MnO_2 powders have been successfully prepared by reaction of potassium permanganate with an organic reductant triethanolamine. And one of the advantages of this method is that $KMnO_4$ is the only source containing manganese. The effect of heat-treatment was studied. The XRD results show a crystalline convert to α-MnO_2 from amorphous MnO_2 when annealed at 400 °C. N_2 adsorptions and desorption studies show higher specific surface area and total pore volume and wider pore size distribution for sample annealed at 350 °C. MnO_2 annealed at 350 °C exhibits a better specific capacitance of 251 F g^{-1} in 1.0 mol L^{-1} Na_2SO_4 electrolyte, which increased 48.5% compared to MN100. The results show that the pseudo-capacitance is obtained depending on the intercalation/deintercalation of cations into the porous bulk of MnO_2 annealed at 350 °C. Good cycle stability characteristic for MnO_2 annealed at 350 °C is also obtained by galvanostatic charging–discharging test.

References

[1] H. Adelkhani, M. Ghaemi, J. Alloys Compd. 493 (2010) 175–178.
[2] J. Li, E.H. Liu, W. Li, X.Y. Meng, S.T. Tan, J. Alloys Compd. 478 (2009) 371–374.
[3] E. Frackowiak, V. Khomenko, K. Jurewicz, K. Lota, F. Beguin, J. Power Sources 153 (2006) 413–418.
[4] W.Y. Kima, M.Y. Kang, J.H. Yi, et al., J. Power Sources 195 (2010) 2125–2129.
[5] H.F. An, Y. Wang, X.Y. Wang, et al., J. Power Sources 195 (2010) 6964–6969.
[6] V. Subramanian, H.W. Zhu, R. Vajtai, P.M. Ajayan, J. Phys. Chem. B 109 (2005) 20207–20214.
[7] R. Liu, S-I.I. Cho, S.B. Lee, Nanotechnology 19 (2008) 215710, 8.
[8] L.M. Li, E.H. Liu, J. Li, Y.J. Yang, J. Power Sources 195 (2010) 1516–1521.
[9] C.H. Liang, C.S. Hwang, J. Alloys Compd. 500 (2010) 102–107.
[10] Y.J. Yang, E.H. Liu, L.M. Li, J. Alloys Compd. 487 (2009) 564–567.
[11] D.P. Dubal, D.S. Dhawalea, C.D. Lokhandea, et al., J. Alloys Compd. 484 (2009) 218–221.
[12] M. Toupin, T. Brousse, Chem. Mater. 16 (2004) 3184–3190.
[13] P. Ragupathy, H.N. Vasan, J. Electrochem. Soc. 155 (2008) A34–A40.
[14] Y. Chen, Y.Z. Hong, Y.P. Ma, et al., J. Alloys Compd. 490 (2010) 331–335.
[15] X.K. Huang, D.P. Lvb, Q.S. Zhang, et al., Electrochim. Acta 55 (2010) 4915–4920.
[16] S.L. Zhao, H.Y. Chen, J. Alloys Compd. 474 (2009) 473–476.
[17] H.J. Guo, X.H. Li, Z.X. Wang, W.J. Peng, X. Cao, H.F. Li, J. Power Sources 189 (2009) 95–100.
[18] L.L. Zhang, T.X. Wei, Micropor. Mesopor. Mater. 123 (2009) 260–267.
[19] F.J. Liu, J. Power Sources 182 (2008) 383–388.
[20] K.W. Nam, C.W. Lee, J. Power Sources 188 (2009) 323–331.
[21] B. Babakhani, D.G. Ivey, J. Power Sources 195 (2010) 2110–2117.
[22] X.L. Hong, G.Y. Zhang, Y.Y. Zhu, Mater. Res. Bull. 38 (2003) 1695–1703.
[23] S. Devaraj, N. Munichandraiah, J. Phys. Chem. C 112 (2008) 4406–4417.
[24] S.B. Ma, Y.H. Lee, K.Y. Ahn, C.M. Kim, K.H. Oh, J. Electrochem. Soc. 153 (2006) C27–C32.
[25] O. Ghodbane, J.L. Pascal, F. Favier, Appl. Mater. Interfaces 1 (2009) 1130–1139.
[26] R.N. Reddy, R.G. Reddy, J. Power Sources 124 (2003) 330–337.
[27] R.N. Reddy, R.G. Reddy, J. Power Sources 132 (2004) 315–320.
[28] J.K. Chang, Y.L. Chen, W.T. Tsai, J. Power Sources 135 (2004) 344–353.
[29] S.E. Chun, Su-I.I. Pyun, G.J. Lee, Electrochim. Acta 51 (2006) 6479–6486.